

Rasterizing Wireless Radiance Field via Deformable 2D Gaussian Splatting

Mufan Liu*, Cixiao Zhang*, Qi Yang, *Member, IEEE*, Yujie Cao, Yiling Xu†, *Member, IEEE*, Yin Xu†, *Senior Member, IEEE*, Shu Sun, *Senior Member, IEEE*, Mingzeng Dai, Yunfeng Guan

Abstract—Modeling the wireless radiance field (WRF) is fundamental to modern communication systems, enabling key tasks such as localization, sensing, and channel estimation. Traditional approaches, which rely on empirical formulas or physical simulations, often suffer from limited accuracy or require strong scene priors. Recent neural radiance field (NeRF)–based methods improve reconstruction fidelity through differentiable volumetric rendering, but their reliance on computationally expensive multilayer perceptron (MLP) queries hinders real-time deployment. To overcome these challenges, we introduce Gaussian splatting (GS) to the wireless domain, leveraging its efficiency in modeling optical radiance fields to enable compact and accurate WRF reconstruction. Specifically, we propose SwiftWRF, a deformable 2D Gaussian splatting framework that synthesizes WRF spectra at arbitrary positions under single-sided transceiver mobility. SwiftWRF employs CUDA-accelerated rasterization to render spectra at over 100k FPS and uses the lightweight MLP to model the deformation of 2D Gaussians, effectively capturing mobility-induced WRF variations. In addition to novel spectrum synthesis, the efficacy of SwiftWRF is further underscored in its applications in angle-of-arrival (AoA) and received signal strength indicator (RSSI) prediction. Experiments conducted on both real-world and synthetic indoor scenes demonstrate that SwiftWRF can reconstruct WRF spectra up to 500x faster than existing state-of-the-art methods, while significantly enhancing its signal quality. Code and datasets will be released.

Index Terms—Ray Tracing, Rendering, Gaussian Splatting, Deep Learning, Wireless Channel Modeling, Channel Estimation.

1 INTRODUCTION

In modern communication systems, digital information is conveyed through radio frequency (RF) waveforms that interact with the physical environment. As they propagate, these signals experience reflection, diffraction, scattering, and absorption, resulting in a continuous and spatially varying signal field (see Fig. 1). Characterizing the spatial–frequency structure of this field forms the foundation of wireless radiance field (WRF) modeling [1], a key area in advancing wireless communication. The motivation for recovering the WRF lies in its ability to encapsulate rich geometric and spectral information, which in turn supports channel estimation, as well as downstream tasks including localization and environmental sensing. Over the years, researchers have explored a wide range of techniques to tackle this problem, from classical Maxwell-based formulations to modern deep neural network approaches. As 6G technologies continue to advance, communication systems in latency-critical domains such as the Internet of Things (IoT) are expected to deliver ultra-reliable, low-latency performance, with end-to-end delays ranging from 10 to 100 microseconds [2], [3]. This makes fast and accurate WRF

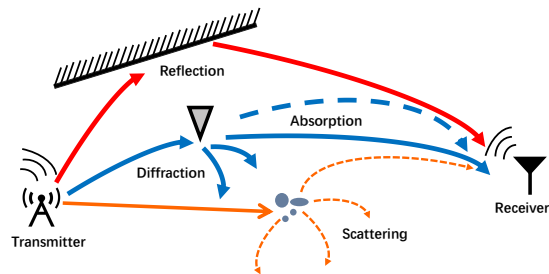


Fig. 1. A toy example of wireless radiance field.

modeling essential for the practical deployment of next-generation wireless systems.

Motivation: Existing approaches to WRF modeling can be broadly categorized into two types: rule-based and learning-based [4]. Rule-based techniques are typically divided into probabilistic and deterministic models. The former rely on empirical formulas calibrated from measurement data to estimate signal strength as a function of transceiver location. While this allows for fast computation, such models often fail to capture fine-grained spatial variations and lack reconstruction fidelity [5], [6]. In contrast, deterministic techniques like ray tracing simulate RF propagation using physical laws, taking into account environmental geometry and material properties. These methods can achieve high accuracy, but their effectiveness hinges on the availability of detailed 3D scene models and comes at a significant computational cost [7]. To overcome the limitations of rule-based methods, learning-based approaches have been developed to reconstruct WRF spectra directly from data using deep neural networks. Classical

• M. Liu, C. Zhang, Y. Cao, Y. Xu, Y. Xu, S. Sun and Y. Guan are from School of Information Science and Electronic Engineering, Shanghai Jiao Tong University, Shanghai, 200240, China (email: {sudo_evan, cixiaozhang, 1452377525, yl.xu, xuyin shusun, yfguan69}@sjtu.edu.cn)

• Q. Yang is with University of Missouri-Kansas City, Kansas, 64110, America (email: qiyang@umkc.edu)

• M. Dai is with Lenovo Group, Lenovo Research, Beijing, 2100094, China (email: {daimz4}@lenovo.com)

(* Authors contribute equally to this work.)

(† Corresponding authors.)

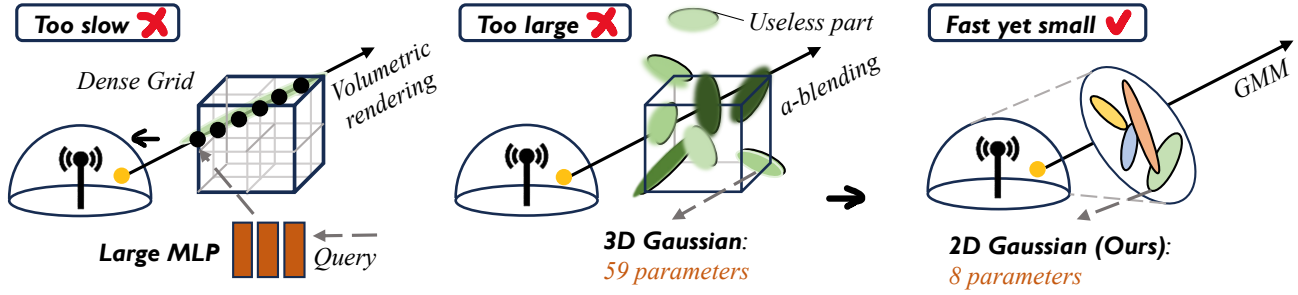


Fig. 2. **Comparison with NeRF-based and GS-based WRF modeling approaches.** NeRF-based solutions rely on computationally intensive volumetric rendering, while 3DGS suffers from dimensional redundancy due to an invariant projection. In contrast, our method achieves both efficiency and compactness by adopting a streamlined 2D Gaussian formulation tailored to the wireless domain.

models such as variational autoencoders (VAEs) [8] and generative adversarial networks (GANs) [9] aim to learn a low-dimensional continuous manifold of the WRF from observed spectra. Once trained, these models can interpolate spectra at arbitrary positions to recover the full field. Despite their improved reconstruction quality, the training process often requires large amounts of high-quality data and offers limited interpretability due to their black-box architectures.

Emerging learning-based studies have drawn connections between WRFs and optical radiance fields, recognizing that both can be modeled as continuous spatial functions based on radiative propagation. This conceptual equivalence has motivated the adaptation of novel view synthesis (NVS) techniques to WRF modeling, where synthesizing spectra at unseen positions is analogous to rendering novel views [10], [11]. A representative example in the NVS domain is neural radiance fields (NeRF) [12], which reconstructs the optical radiance field from sparse views via multilayer perceptron (MLP)-based volumetric rendering. Building on this idea, [13], [14], [15] extend the NeRF framework to the wireless domain, achieving impressive spectra reconstruction fidelity by implicitly modeling the underlying WRF structure. However, their accuracy comes at the cost of expensive MLP queries for field density, which significantly slows down inference and limits their suitability for latency-sensitive applications.

Recent advances in NVS have seen Gaussian splatting (GS) [16] achieves notable progress in both efficiency and rendering quality. Unlike NeRF-based methods that rely on neural volumetric rendering, GS models a scene as a set of anisotropic 3D Gaussian primitives with explicit geometric and radiance attributes. These primitives collectively approximate the underlying optical radiance field and render novel views via differentiable rasterization. A key strength of the GS pipeline lies in its CUDA-accelerated parallel implementation, which enables differentiable rasterization to be efficiently performed in a tile-wise manner. By avoiding computationally expensive volumetric ray marching, GS significantly reduces both training and inference overhead while preserving photorealistic rendering. Motivated by its efficiency in modeling optical radiance fields, we aim to adopt the GS technique to tackle the remaining challenges in WRF. Yet, our analysis reveals several limitations in its direct application to the WRF domain, as outlined below to motivate our redesign.

Observation: To our knowledge, existing GS-based methods [4], [17] have been applied primarily to WRF scenarios with one moving transmitter (TX) and one fixed receiver (RX). At each TX position, the RX records a spatial spectrum synthesized via differentiable rasterization of a set of 3D Gaussians, with their attributes dynamically predicted from the TX’s location. While this design improves inference efficiency, we identify several limitations that restrict its applicability in the wireless domain: *First, the use of a 3D volumetric representation is unnecessary.* The 3D Gaussian formulation captures spatial variations critical in NVS, but such variations are absent in WRF under TX-side mobility. In this setting, TX movement induces only a global shift of the 3D Gaussian splatting (3DGS) field, without introducing any spatial variation in its projection from the RX side. As the projection remains constant, we posit that modeling the 2D projection of 3D Gaussian directly may serve as an equally effective solution. *Second, existing methods lack locality-aware modeling.* In [4], Gaussian attributes are predicted independently at each TX location, without accounting for spatial correlations among neighboring positions [4]. This position-wise formulation overlooks the continuity of the underlying physical field, potentially leading to suboptimal convergence and poor generalization [18]. *Third, sparse supervision introduces a risk of overfitting.* Existing methods optimize quality loss only over observed regions, without applying any regularization to unobserved areas. This lack of supervision hinders the model’s ability to interpolate and generalize to unseen positions. *Fourth, limited evaluation settings.* Existing methods are typically tested on a single scene under the TX-moving configuration (NeRF² – s23 dataset [13]). The lack of diverse scenes, i.e., RX-moving cases, limits the credibility of their results.

Together, these limitations constrain the scalability, generalization, and physical alignment of existing GS-based WRF modeling approaches. In response, we propose a streamlined GS framework tailored to the structural and physical characteristics of the WRF, and enabling evaluation across both TX- and RX-moving scenarios.

Our method: We propose a deformable 2D Gaussian splatting (2DGS) framework, termed *SwiftWRF*, to address WRF reconstruction under single-sided transceiver¹ mobility. The method begins by formulating a 2D Gaussian representation tailored to the wireless domain, where each

1. Refers to either the moving TX or RX, depending on the scenario.

primitive captures localized signal behavior through a 2D Gaussian distribution and a complex-valued response. To render the spatial spectrum, we adopt a Gaussian mixture model (GMM)-like formulation [19], in which all 2D Gaussian primitives are directly blended over the plane via differentiable rasterization. Compared to 3D Gaussians, our 2D formulation substantially improves compactness, reducing the parameter count by a factor of seven, as illustrated in Fig. 2. The blending process also eliminates the need for camera projection and removes dependence on geometry-based initialization. Complementing this, transceiver mobility is modeled through a continuous deformation field, implemented as a lightweight MLP that predicts position-dependent offsets to a global set of 2D Gaussian parameters. This design enables fast, spatially coherent adaptation across locations, aligning more closely with the physical characteristics of WRF. To improve generalization and mitigate overfitting, we incorporate an annealed smoothing mechanism that injects controlled positional noise during training, with its magnitude decaying exponentially as training progresses.

For evaluation, we construct a synthetic dataset to assess the generality of *SwiftWRF* beyond TX-moving settings. The dataset includes both TX-moving and RX-moving scenarios, spanning three representative indoor layouts, with spectra generated using MATLAB’s ray-tracing toolbox. Extensive experiments show that *SwiftWRF* achieves a peak signal-to-noise ratio (PSNR) improvement of 2.33–10.41 dB over existing baselines, while delivering inference speeds of approximately 100k FPS—over 500× faster than WRF-GS and more than 20,000× faster than NeRF². Finally, we evaluate *SwiftWRF* on two case studies. For angle-of-arrival (AoA) prediction, the synthesized spectra are integrated into a turbo-learning framework, where they serve as augmented data to enhance estimation accuracy. For received signal strength indicator (RSSI) prediction, we adapt the rendering head with average pooling to support scalar field regression. These case studies validate the generalizability of our method and demonstrate consistent improvements over existing baselines.

To summarize, our contributions are as follows:

- We propose a compact and efficient 2DGS representation tailored to WRF modeling, which replaces the unnecessary 3D structure and spherical harmonics used in prior methods.
- We introduce a deformation field module parameterized by a lightweight MLP to effectively capture transceiver-induced variations across space, along with an annealed smoothing strategy to enhance generalization.
- We construct and release a synthetic WRF dataset covering both TX-moving and RX-moving scenarios, generated using MATLAB’s ray-tracing toolbox over multiple representative indoor environments.
- We extensively evaluate our method on WRF reconstruction and two downstream tasks, AoA and RSSI prediction, and demonstrate significant gains in both accuracy and efficiency.

The remainder of this paper is organized as follows. Section 2 reviews related work on GS and wireless radiance

fields. Section 3 introduces necessary preliminaries and formalizes the problem statement. Section 4 details the proposed *SwiftWRF* framework for WRF modeling under single-sided mobility. Section 5 describes the construction of our synthetic spectrum dataset. Section 6 presents the experimental setup and evaluation results. Section 7 shows two case studies, and Section 8 concludes the paper and outlines future research directions.

2 RELATED WORK

Our work falls within the domain of WRF modeling and channel parameter prediction, and intersects with the emerging area of GS.

2.1 Wireless Radiance Field Modeling

WRF modeling seeks to characterize electromagnetic wave propagation between TXs and RXs, incorporating reflection, diffraction, scattering, and path-loss effects [20], [21]. Conventional approaches to channel modeling can be broadly classified into two categories: probabilistic models and deterministic ray-tracing models. The former are computationally efficient and easy to implement; however, they often fail to capture fine-grained spatial variations and site-specific details [22]. The latter offer high-fidelity, site-specific predictions by modeling the exact propagation environment [1], but they are computationally intensive and require detailed prior knowledge of the geometric layout, which limits their scalability and applicability in dynamic or unknown environments. Learning-based methods instead train deep networks on extensive, location-tagged channel measurements to directly infer complex propagation phenomena [8], [9], but they often lack interpretability and struggle to generalize beyond their training distributions. More recently, NeRF-based methods have been applied to learn WRF as an optical field [13], [14], [23]. Zhao et al. [13] developed NeRF² for spatial-spectrum reconstruction in real environments; Orekondy et al. [23] introduced a NeRF surrogate for indoor EM propagation using synthetic datasets; and Lu et al. [14] proposed NeWRF, which predicts channel states from sparse measurement sets. Considering the slow rendering of NeRF, a few GS-based methods model WRF with explicit Gaussian primitives and leverage CUDA-accelerated rasterization to synthesize spectra in near real time [4], [17]. However, these approaches remain rudimentary 3D GS frameworks and lack the specialized design needed to meet the stringent requirements of ultra-reliable low-latency communication (URLLC). To address this gap, we present *SwiftWRF*, an efficient 2DGS framework that simultaneously achieves faster training and inference times, alongside superior reconstruction fidelity.

2.2 Channel Parameter Prediction

RSSI prediction: RSSI prediction estimates signal strength across a venue from limited measurements, underpinning coverage planning and indoor localization. Shin et al. [24] proposed MRI, a smartphone-based system that interpolates indoor RSSI via a log-distance path-loss model and sparse war-walking data. Zhao et al. [13] developed a NeRF²-based, turbo-learning RSSI predictor using the public BLE

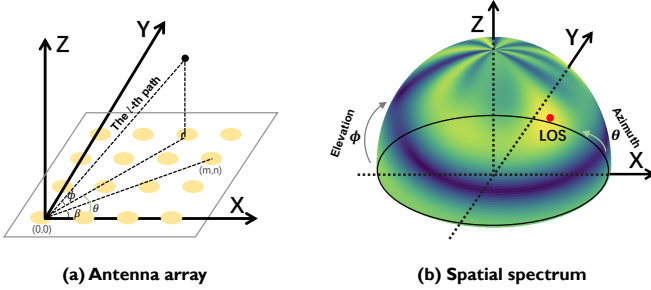


Fig. 3. Illustration of RX (origin) antenna array (a) and spatial spectrum (b).

dataset [13]. We similarly retrain SwiftWRF on that dataset to evaluate its RSSI prediction performance.

AoA prediction: AoA prediction estimates the direction of line-of-sight (LOS) propagation by identifying the peak in the spatial spectrum, serving as a critical component for accurate indoor localization. However, the task remains highly challenging due to multipath propagation and destructive interference of varying wireless conditions. To address this issue, iArk’s AoA Neural Network (AANN) [25] corrects spectral peak deviations via deep learning but requires large volumes of high-quality data. NeRF²’s turbo-learning strategy [13] alleviates this by synthesizing spatial spectra to augment the training set. Building on these, we apply the turbo-learning strategy to the synthesized dataset generated by SwiftWRF and retrain AANN on a mixed dataset generated by SwiftWRF, which yields cleaner spectra and further boosts AoA prediction in complex wireless scenarios.

2.3 Gaussian Splatting

GS has recently emerged as a powerful technique for novel-view synthesis, employing explicit 3D Gaussian primitives and differentiable, tile-based rasterization to achieve real-time rendering and interactive editing capabilities [16], [26]. Its efficacy has motivated extensions to dynamic scene modeling [18], [27], AI-driven content creation [28], autonomous driving [29], and wireless communication [4], [17], [30]. Although initially developed for 3D applications, the principles of GS have also been extended to 2D domains [31]. For example, GaussianImage [19] represents images using 2D Gaussian kernels to enable rapid decoding, while Hu et al. [32] employ 2D Gaussians to model precise mesh geometry. To our knowledge, SwiftWRF is the first framework to leverage 2DGS for efficient WRF modeling. Across multiple indoor scenarios, SwiftWRF delivers state-of-the-art reconstruction accuracy and furthermore facilitates downstream RF tasks such as AoA and RSSI prediction.

3 PRELIMINARY AND PROBLEM FORMULATION

In this section, we first review the core principles of WRF and formalize the WRF modeling problem under single-sided transceiver mobility. We then introduce the key concepts of GS that are adapted to the WRF domain.

3.1 Wireless Radiance Field

A typical wireless communication link involves a TX and an RX that exchange information via RF signals. The TX emits an RF waveform that propagates through space and eventually reaches the RX. During propagation, the signal interacts with the environment through reflection, diffraction, scattering, and absorption. These interactions give rise to multiple propagation paths, whose superposition at different spatial locations forms a spatially varying and complex electromagnetic field—known as the WRF.

To extract directional information from this field, the RX is typically equipped with an antenna array composed of spatially distributed elements. By adjusting the phase or timing of the signals received at each element, the array can steer its sensitivity toward a desired direction, effectively forming a narrow reception beam. Sweeping across angles allows the RX to measure signal energy from multiple directions and aggregate these measurements into a spatial spectrum, as illustrated in Fig. 3.

Spatial spectrum: Consider an RX equipped with a two-dimensional $\sqrt{K} \times \sqrt{K}$ antenna array with element spacing D , as illustrated in Fig. 3. The (m, n) -th antenna element, denoted $R_{m,n}$, is located at a position specified by its polar coordinates. Its radial and angular coordinates are defined as

$$\begin{cases} r_{m,n} = D\sqrt{(m-1)^2 + (n-1)^2}, \\ \beta_{m,n} = \arctan 2(m-1, n-1). \end{cases} \quad (1)$$

Assuming L_p multipath components, the channel at $R_{m,n}$ is

$$h_{m,n} = \sum_{l=1}^{L_p} \rho_l e^{j\Delta\alpha_{m,n}(\theta_l, \phi_l)}, \quad (2)$$

where ρ_l is the power coefficient associated with the l -th propagation path, and θ_l, ϕ_l denote its azimuth and elevation angles, respectively. The phase difference is expressed as

$$\begin{aligned} \Delta\alpha_{m,n}(\theta, \phi) &= \alpha_{m,n}(\theta, \phi) - \alpha_{1,1}(\theta, \phi) \\ &= 2\pi\Delta d_{m,n}(\theta, \phi)/\lambda \pmod{2\pi} \\ &= -2\pi r_{m,n} \cos(\theta - \beta_{m,n}) \cos(\phi)/\lambda \pmod{2\pi}. \end{aligned} \quad (3)$$

Here, $\Delta d_{m,n}$ is the path length difference between antennas $R_{m,n}$ and $R_{1,1}$ along direction (θ, ϕ) , and λ denotes the signal wavelength. The RX estimates the spatial spectrum by applying an analog combining matrix that steers beams toward predefined azimuth θ and elevation ϕ angles. When a beam aligns with the true AoA, signals from that direction combine constructively, while signals from other directions interfere destructively and are attenuated [25]. The spatial spectrum at direction (θ, ϕ) is then computed as

$$\mathbf{A}(\theta, \phi) = \left| \frac{1}{K} \sum_{m=1}^{\sqrt{K}} \sum_{n=1}^{\sqrt{K}} w_{m,n}(\theta, \phi) e^{j\angle h_{m,n}} \right|, \quad (4)$$

where $w_{m,n}(\theta, \phi) = e^{-j\Delta\alpha_{m,n}(\theta, \phi)}$ is the complex weight for steering a beam to a certain angle of (θ, ϕ) applied to the (m, n) -th antenna element. Under our assumption of 1°

angular resolution, the spatial spectrum is represented as a 360×90 matrix \mathbf{A} , defined by

$$\mathbf{A} = \begin{bmatrix} \mathbf{A}(0^\circ, 0^\circ) & \mathbf{A}(1^\circ, 0^\circ) & \cdots & \mathbf{A}(359^\circ, 0^\circ) \\ \mathbf{A}(0^\circ, 1^\circ) & \mathbf{A}(1^\circ, 1^\circ) & \cdots & \mathbf{A}(359^\circ, 1^\circ) \\ \vdots & \vdots & \ddots & \vdots \\ \mathbf{A}(0^\circ, 89^\circ) & \mathbf{A}(1^\circ, 89^\circ) & \cdots & \mathbf{A}(359^\circ, 89^\circ) \end{bmatrix}. \quad (5)$$

The spatial spectrum represents a spatial power distribution function that directly captures the propagation behavior of RF signals through the environment. As such, it is commonly used as an effective representation of the WRF.

3.2 Problem Formulation

We consider the problem of WRF reconstruction under *single-sided transceiver mobility*, where exactly one TX and one RX are placed in an indoor scene. In this setting, either the TX or the RX moves while the other remains fixed, giving rise to two distinct scenarios:

TX-moving scenario. The TX moves across a set of known positions

$$\mathcal{P} = \{\mathbf{p}_i \in \mathbb{R}^3\}_{i=1}^{N_s},$$

and emits WRF signals at each location, while the RX remains fixed at $\mathbf{q} \in \mathbb{R}^3$ to collect the corresponding spectra $\{\mathbf{A}_i\}_{i=1}^{N_s}$. Here, N_s denotes the number of TX positions.

RX-moving scenario. The TX emits WRF signals from a fixed position $\mathbf{p} \in \mathbb{R}^3$, while the RX moves across a set of known positions

$$\mathcal{Q} = \{\mathbf{q}_i \in \mathbb{R}^3\}_{i=1}^{N_s},$$

and collects the corresponding spectra $\{\mathbf{A}_i\}_{i=1}^{N_s}$. Again, N_s denotes the number of RX positions.

The indoor scene is assumed to exhibit rich multipath propagation. To prevent Doppler effects, the moving transceiver remains stationary during each spectrum acquisition. At each position $\mathbf{s}_i \in \mathcal{P}$ (\mathcal{Q} for RX-moving), the spectrum is collected by RX as a discrete angular spectrum matrix

$$\mathbf{A}_i = [\mathbf{A}_i(\theta_j, \phi_k)] \in \mathbb{C}^{M_\theta \times M_\phi},$$

where M_θ and M_ϕ denote the number of angular samples in the azimuth and elevation directions, respectively. The angular grids are given by $\{\theta_j\}_{j=1}^{M_\theta} \subset [0, 2\pi)$ and $\{\phi_k\}_{k=1}^{M_\phi} \subset [0, \frac{\pi}{2}]$. Let

$$\{(\mathbf{s}_i, \mathbf{A}_i)\}_{i=1}^{N_s}, \quad \mathbf{s}_i \in \begin{cases} \mathcal{P}, & \text{TX-moving,} \\ \mathcal{Q}, & \text{RX-moving,} \end{cases}$$

denote the collected spectra paired with their corresponding transceiver positions. The objective is to learn a continuous mapping

$$\mathcal{F}: \mathbb{R}^3 \rightarrow \mathbb{C}^{M_\theta \times M_\phi}, \quad \mathbf{s} \mapsto \mathcal{F}(\mathbf{s}),$$

such that for any novel position $\mathbf{s}_{\text{new}} \notin \mathcal{P}$ (\mathcal{Q} for RX-moving), the prediction $\mathcal{F}(\mathbf{s}_{\text{new}})$ closely approximates the true spatial spectrum.

3.3 Gaussian Splatting

GS originally refers to the 3DGS framework, which performs NVS through CUDA-based differentiable rasterization. Beyond its success on NVS benchmarks, its 2D extension (2DGS) enables more compact representations of 2D surfaces, including images, meshes, and point-based geometry. Since the WRF is received in the form of a 2D spatial spectrum, it is naturally constructed using a 2D Gaussian-based formulation for improved efficiency. To motivate this choice, the following section first reviews the 3DGS framework, followed by a description of the 2DGS.

3D Gaussian: 3DGS reconstructs unseen views of a 3D scene by training a set of Gaussian primitives from a sparse collection of captured images. These primitives are positioned in free 3D space, with each representing a small, smooth region characterized by a set of learnable attributes: a mean position $\boldsymbol{\mu} \in \mathbb{R}^3$, a covariance matrix $\boldsymbol{\Sigma} \in \mathbb{R}^{3 \times 3}$, an opacity value $\alpha \in [0, 1]$ indicating transparency, and a color vector $\mathbf{c} \in \mathbb{R}^k$ encoding appearance via spherical harmonics (SH) coefficients. Each Gaussian primitive models the likelihood of a point $\mathbf{x} \in \mathbb{R}^3$ belonging to its region, following a 3D Gaussian distribution defined as

$$\mathbf{G}(\mathbf{x}) = \exp\left(-\frac{1}{2}(\mathbf{x} - \boldsymbol{\mu})^\top \boldsymbol{\Sigma}^{-1}(\mathbf{x} - \boldsymbol{\mu})\right). \quad (6)$$

For rendering, primitives are sorted by depth in camera space and projected through the camera matrix onto the image plane, producing 2D Gaussian footprints. These footprints are blended front to back: closer primitives contribute first, while more distant ones are attenuated by the accumulated opacity. At each pixel, the color C is obtained by α -blending all overlapping footprints along the viewing ray

$$C = \sum_{i=1}^N \mathbf{c}_i \alpha_i \prod_{j=1}^{i-1} (1 - \alpha_j), \quad (7)$$

where \mathbf{c}_i and α_i denote the color and opacity of the i -th primitive, respectively, and N is the number of primitives affecting the pixel. This process is known as differentiable rasterization, as it enables the optimization of Gaussian attributes through gradient backpropagation based on the end-to-end rendering loss.

2D Gaussian: While modeling the full WRF is inherently a 3D problem, synthesizing the RX's spatial spectrum does not require 3D projection and can be captured more efficiently using 2D Gaussian primitives. In 2DGS, each Gaussian primitive is parameterized by a 2D position $\boldsymbol{\mu} \in \mathbb{R}^2$, a 2D covariance matrix $\boldsymbol{\Sigma} \in \mathbb{R}^{2 \times 2}$, and a DC color vector $\mathbf{c} \in \mathbb{R}^3$. Higher-order spherical harmonics coefficients are discarded as the viewpoint is fixed in the 2D setting. To ensure the positive semi-definiteness of $\boldsymbol{\Sigma}$ and maintain numerical stability during optimization, a Cholesky factorization is employed, where the covariance matrix is decomposed as $\boldsymbol{\Sigma} = \mathbf{L}\mathbf{L}^\top$, with $\mathbf{L} \in \mathbb{R}^{2 \times 2}$ being a lower triangular matrix parameterized by $\mathbf{l} = \{l_1, l_2, l_3\}$. To render a 2D image, the color C at each pixel is computed by aggregating the contributions from all nearby Gaussians N , following

$$C = \sum_{n=1}^N \mathbf{c}_n \cdot \exp\left(-\frac{1}{2}\mathbf{d}_n^\top \boldsymbol{\Sigma}_n^{-1} \mathbf{d}_n\right), \quad (8)$$

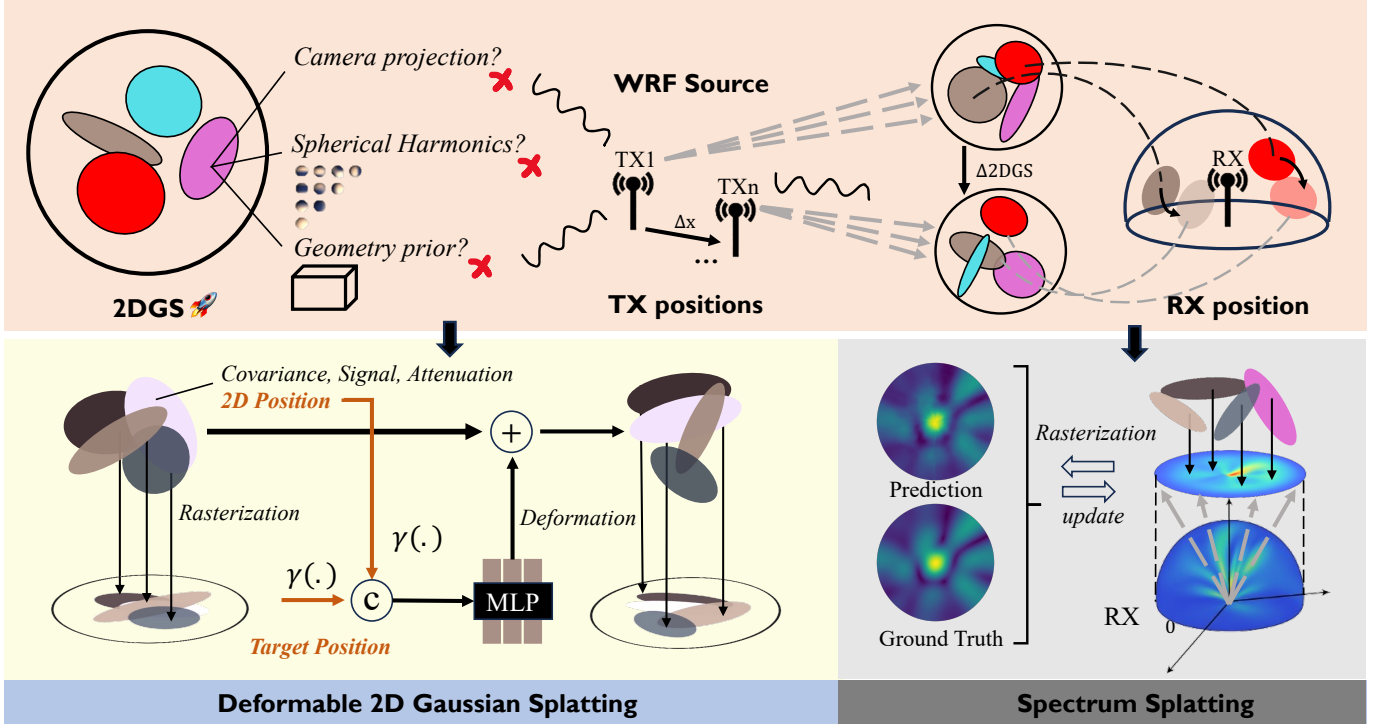


Fig. 4. Overview of SwiftWRF. For illustration, we present the operating pipeline for the TX-moving scenario (top). The bottom left depicts the architecture of deformable 2DGS, while the bottom right illustrates the spectrum rasterization process.

where $\mathbf{d}_n = \mathbf{x}_i - \boldsymbol{\mu}_n$ denotes the displacement between the pixel location \mathbf{x}_i and the center of the n -th Gaussian.

3.4 Summary

To summarize, we describe the formulation of spatial spectrum and define our problem setup under single-sided transceiver mobility. We also outline the GS technique, particularly its 2D extension, which forms the basis of our proposed framework. The observation that WRF spectra share the same 2D structural nature as images motivates our choice of 2D Gaussians. Building on this formulation, the next section addresses the modality gap between images and spectra, and details how our framework incorporates transceiver mobility.

4 METHOD

In this section, we present the SwiftWRF architecture for modeling WRF under single-sided transceiver mobility. We first formulate a 2D Gaussian representation to construct spatial spectra, then introduce a deformation mechanism to capture their dynamics during transceiver mobility. Finally, we describe a two-stage training protocol and key optimization strategies. The following subsections detail each component.

4.1 WRF Modeling via 2DGS

Under single-sided mobility, one transceiver is allowed to move, and a spatial spectrum is collected at each position where it stops. To model a collected spectrum $\mathbf{A}(\phi, \theta)$, we reformulate the 2D Gaussian formulation from Sec. 3.2 to

the wireless domain and introduce a spatial rasterization process based on its original rasterization procedure.

2D Gaussian for WRF: In WRF, each 2D Gaussian primitive provides a localized representation of the signal, exhibiting a peak response at its center and decaying according to its associated Gaussian distribution. This distribution is parameterized by an angular center $\boldsymbol{\mu}_n = (\phi, \theta)$ and a covariance matrix $\boldsymbol{\Sigma}_n \in \mathbb{R}^{2 \times 2}$. To model the WRF signal response, we introduce an attenuation factor $\delta_n \in \mathbb{R}$ to control amplitude decay, and a signal vector $\boldsymbol{\psi}_n \in \mathbb{R}^2$ to represent the real and imaginary parts of the complex-valued response. The angular center is normalized to lie within the valid spectrum range using a hyperbolic transformation:

$$\tilde{\theta} = \frac{\pi}{4} (\tanh(\theta) + 1), \quad \tilde{\phi} = \pi (\tanh(\phi) + 1).$$

The covariance matrix $\boldsymbol{\Sigma}_n$ is parameterized through its Cholesky factor \mathbf{l}_n (see Sec. 3.2). The attenuation factor is defined as $\delta_n = \sigma(a_n)$, where $a_n \in \mathbb{R}$ is a learnable scalar and $\sigma(\cdot)$ denotes the sigmoid function. This gating mechanism regulates the contribution of each primitive to the reconstructed spectrum and helps prevent gradient explosion during optimization.

Spectrum Rasterization: The localized signal representations described above are aggregated into a spectrum using a GMM framework. For each primitive, a Gaussian kernel weight \mathcal{K} is computed to modulate its signal response $\boldsymbol{\psi}$, and the final spectrum value is obtained by summing the modulated responses from all primitives. Specifically, the kernel weight of the n -th primitive at the direction (ϕ, θ) is computed as

$$\mathcal{K}(\boldsymbol{\mu}_n, \boldsymbol{\Sigma}_n, \delta_n) = \delta_n \cdot \exp\left(-\frac{1}{2} \mathbf{d}_n^\top \boldsymbol{\Sigma}_n^{-1} \mathbf{d}_n\right), \quad (9)$$

where $\mathbf{d}_n = (\phi - \phi_n, \theta - \theta_n)$ denotes the displacement between the direction (ϕ, θ) and the primitive center $\boldsymbol{\mu}_n$. The scalar δ_n represents the attenuation factor of the primitive, while the exponential term $\exp\left(-\frac{1}{2}\mathbf{d}_n^\top \boldsymbol{\Sigma}_n^{-1} \mathbf{d}_n\right)$ evaluates the likelihood that the sample at (ϕ, θ) falls within the influence of that primitive. Utilizing the kernel to modulate each primitive's signal response ψ_n , the spectrum value at (ϕ, θ) is computed as

$$\mathbf{A}(\phi, \theta) = \sum_{n \in \mathcal{N}} \psi_n \cdot \mathcal{K}(\boldsymbol{\mu}_n, \boldsymbol{\Sigma}_n, \delta_n). \quad (10)$$

Drawing inspiration from differentiable rasterization, we refer to this process as *spectrum rasterization*. The 2D Gaussian parameters are optimized iteratively through gradient back-propagation, guided by the loss between the predicted and ground-truth spectra. The entire pipeline is implemented in CUDA, with the spectrum domain partitioned into parallel tiles to fully exploit GPU acceleration.

4.2 Deforming 2DGS for WRF Modeling under Mobility

The spectrum rasterization described in Sec. 4.1 defines a one-to-one mapping between the spatial spectrum domain and the 2DGS domain. As the transceiver moves across positions $\mathbf{s} \in \mathcal{S}$, the resulting spectra $\{\mathbf{A}^s\}_{s \in \mathcal{S}}$ can be equivalently represented as a 2DGS *video* $\{\mathcal{G}^s\}_{s \in \mathcal{S}}$, where the frame \mathcal{G}^s consists of a set of 2D Gaussians

$$\mathcal{G}^s = \{(\boldsymbol{\mu}_n^s, \boldsymbol{\Sigma}_n, \psi_n^s, \delta_n^s)\}_{n=1}^N, \quad \mathbf{s} \in \mathcal{S}. \quad (11)$$

We assume a constant number of primitives N across all frames and note that applying spatial rasterization to \mathcal{G}^s yields the corresponding spectrum \mathbf{A}^s . To avoid the redundant per-frame 2DGS modeling, a Group-of-Pictures (GOP) paradigm is proposed: a global parameter set is first constructed as a *reference frame* \mathcal{G}^0 , and each subsequent frame is represented by primitive-wise residuals

$$\Delta \mathcal{G}^s = \{(\Delta \boldsymbol{\mu}_n^s, \Delta \psi_n^s, \Delta \delta_n^s)\}_{n=1}^N. \quad (12)$$

The primitive set at position \mathbf{s} is then given by

$$\mathcal{G}^s = \{(\boldsymbol{\mu}_n^0 + \Delta \boldsymbol{\mu}_n^s, \boldsymbol{\Sigma}_n, \psi_n^0 + \Delta \psi_n^s, \delta_n^0 + \Delta \delta_n^s)\}_{n=1}^N, \quad (13)$$

where $\Delta \boldsymbol{\mu}_n^s$, $\Delta \psi_n^s$, and $\Delta \delta_n^s$ denote the residuals in position, response, and attenuation for the n th Gaussian primitive at moving location \mathbf{s} . The residuals on the covariance matrices are omitted to preserve the triangular structure required by Cholesky factorization. Therefore, the spectrum rasterization under single-sided mobility generalizes to

$$\mathbf{A}^s(\phi, \theta) = \sum_{n \in \mathcal{N}} (\psi_n^0 + \Delta \psi_n^s) \cdot \mathcal{K}(\boldsymbol{\mu}_n^0 + \Delta \boldsymbol{\mu}_n^s, \boldsymbol{\Sigma}_n^0, \delta_n^0 + \Delta \delta_n^s). \quad (14)$$

However, modeling spectrum variations as residuals captures only discrete offsets at sampled positions $\mathbf{s} \in \mathcal{S}$, and fails to generalize to unseen locations $\mathbf{s}_{\text{new}} \notin \mathcal{S}$. To overcome this limitation, we introduce a continuous deformation field², implemented as a lightweight MLP that maps any moving position to the corresponding primitive residuals (see Fig. 4 bottom left). Concretely, it predicts

2. We use “deformation” to denote continuous variation and “residual” for discrete offsets.

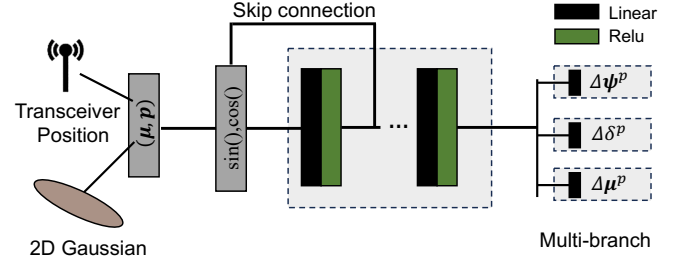


Fig. 5. Structure of the deformation MLP.

residuals for three components: First, $\Delta \boldsymbol{\mu}_n^s$ represents the motion vector of each primitive, capturing translational shifts caused by transceiver mobility. Second, $\Delta \psi_n^s$ refines the signal response through a residual map that encodes fine-scale variations. Third, $\Delta \delta_n^s$ adjusts the attenuation factor to account for phenomena such as path blockage or reappearance. The deformation MLP takes the positional encodings of each primitive center $\boldsymbol{\mu}$ and the moving position \mathbf{s} as input, and predicts their residuals as

$$\Delta \boldsymbol{\mu}_n^s, \Delta \psi_n^s, \Delta \delta_n^s = \mathcal{F}_\theta(\gamma(\boldsymbol{\mu}_n), \gamma(\mathbf{s})), \quad (15)$$

where \mathcal{F}_θ is the deformation MLP with parameters θ , and $\gamma(\cdot)$ denotes the positional encoding function. Given an input vector $\mathbf{s} \in \mathbb{R}^d$, the embedding is defined as:

$$\gamma(\mathbf{s}) = \left[\mathbf{s}, \{\sin(2^k \pi \mathbf{s})\}_{k=0}^{L-1}, \{\cos(2^k \pi \mathbf{s})\}_{k=0}^{L-1} \right]. \quad (16)$$

Here, each sine and cosine function is applied element-wise to all dimensions of \mathbf{s} , and L denotes the number of frequency bands. This yields a total embedding dimension of $d(2L + 1)$. Introducing multiple frequency bands allows the MLP to capture both coarse and fine-grained variations in the WRF.

4.3 SwiftWRF

As illustrated in Fig. 4, combining the 2D Gaussian formulation with the deformation MLP yields our complete model, *SwiftWRF*. In this unified framework, each primitive and the transceiver position are jointly input to the deformation MLP, which outputs per-primitive offsets. The deformed primitives are then passed through a CUDA-accelerated spatial rasterization pipeline to synthesize the target spectrum. This design integrates the efficiency of GS with the flexibility of a learnable continuous deformation field, enabling fast and accurate end-to-end WRF reconstruction without relying on volumetric grids.

4.4 Training Protocol

Coarse to fine training: SwiftWRF adopts a two-stage coarse-to-fine training protocol, which is more efficient than training the full model from scratch. In the coarse stage, only the 2D Gaussian primitives are optimized to fit the entire set of measured spectra, while the deformation network remains frozen. This stage establishes a shared representation for the reference 2DGS frame and converges within seconds. In the fine stage, the deformation MLP is activated to learn adjustments conditioned on the location of the

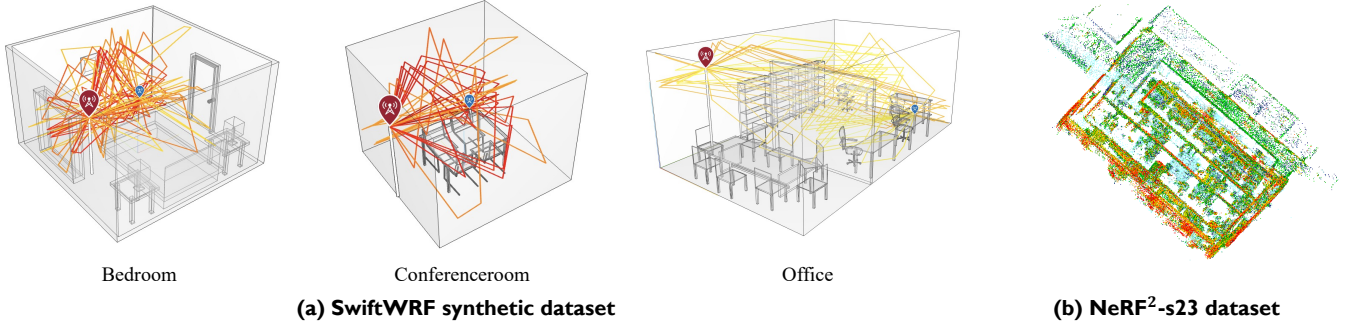


Fig. 6. Geometry overview of the real-world (b) and synthetic dataset scenes (a).

moving transceiver. To stabilize training, gradients to the primitive positions are frozen, concentrating optimization on the signal response variations.

Loss function: The goal of the training protocol is to reconstruct the spectrum at each moving position by minimizing the discrepancy between the predicted and ground-truth spectra. To achieve this, we use a hybrid loss function that combines the ℓ_1 loss with the Structural Similarity Index Measure (SSIM) loss:

$$\mathcal{L} = \lambda_1 \cdot \|\hat{\mathbf{A}}^s - \mathbf{A}^s\|_1 + (1 - \lambda_1) \cdot (1 - \text{SSIM}(\hat{\mathbf{A}}^s, \mathbf{A}^s)), \quad (17)$$

where $\hat{\mathbf{A}}^s$ is the reconstructed spectrum at position s , \mathbf{A}^s is the ground-truth spectrum, and λ_1 is a scalar weight balancing the contributions of the two terms. The ℓ_1 loss promotes pixel-wise accuracy, while the SSIM term encourages local structural similarity, ensuring both fidelity and spatial consistency in WRF reconstruction.

Anneal Smoothing: The training loss defined in the previous subsection does not impose any smoothness across different positions, which can easily lead to overfitting, i.e., poor results when reconstructing spectra at unseen locations. To address this, we adopt an anneal smoothing strategy [18], where random Gaussian noise \mathbf{n}_i is added to the position s at each iteration i and gradually decays over the course of training. With slight abuse of notation, we denote the deformation components by Δ after applying anneal smoothing. The procedure is formulated as:

$$\Delta = \mathcal{F}_\theta(\gamma(\boldsymbol{\mu}), \gamma(s + \mathbf{n}_i)), \quad (18)$$

$$\mathbf{n}_i = \gamma \cdot \mathcal{N}^3(0, 1) \cdot \frac{2}{\sqrt[3]{N_s}} \cdot \left(1 - \frac{i}{\tau}\right). \quad (19)$$

Here, γ is a scaling factor, and $\mathcal{N}^3(0, 1)$ denotes a standard 3D normal distribution. The term $\frac{2}{\sqrt[3]{N_s}}$ approximates the sampling interval, assuming that the N_s positions are uniformly distributed within a normalized unit cube. The parameter τ denotes the iteration threshold for annealing. Introducing position smoothness improves SwiftWRF's generalization in the early stages of training, while gradually reducing its influence helps prevent excessive smoothing in later stages. Meanwhile, this regularization mitigates jitter artifacts during position interpolation by the deformation MLP.

TABLE 1
Hyperparameter setting.

Symbol	Meaning	Value
γ	Anneal smoothing weight	1
τ	Anneal smoothing threshold	10k
ϵ_g	Gaussian learning rate	1e-2
ϵ_m	MLP learning rate	8e-3
λ_1	l1 loss weight	0.7

5 SYNTHETIC SPECTRA VIA RAY-TRACING

We employ the ray tracing module from MATLAB's Communications Toolbox [33], [34] to generate a corpus of spatial spectra across three representative indoor environments [14]: *conference room*, *office*, and *bedroom* (see Fig. 6 (a)), each simulated under two single-sided transceiver mobility configurations: 1) the TX is fixed and RX is placed at multiple positions to collect spectra, and 2) the RX is fixed to receive spectra from TX placed at multiple positions. These two configurations are among the most common in wireless communication and reflect typical use cases.

The ray-tracing module employs the shooting and bouncing rays (SBR) method to simulate realistic wireless propagation. For each scene, it launches rays from a TX toward its RX location in the scene's geometry model (e.g., mesh or CAD files) and computes specular reflections, diffraction, scattering, and path loss for each valid propagation path. The RX records channel responses, including AoA and multipath components, for the purpose of spectrum measurement. For each path, the phase shift is computed using Eq.(3), and the overall channel is synthesized via superposition as described in Eq.(2). Finally, directional beam scanning is performed by sweeping across the angular directions defined in Eq. (4) to construct the spatial spectrum. Depending on the configuration, we place either the TX or the RX through multiple positions and repeat the SBR process, producing about 6,000 spectra per scene.

6 EXPERIMENT

6.1 Implementation Details

We evaluate SwiftWRF on both real-world and synthetic datasets, and demonstrate its versatility on two case studies: AoA prediction and RSSI prediction. Spectrum rasterization is implemented on top of the open-source Gsplat framework [35] that allows CUDA-based parallel processing. The

TABLE 2
Comparison of methods on different scenes (Median PSNR↑, SSIM↑ and mean L1↓).

Method	Conferenceroom (TX-moving)			Bedroom (TX-moving)			Office (TX-moving)			NeRF ² -s23		
	PSNR↑	SSIM↑	L1↓	PSNR↑	SSIM↑	L1↓	PSNR↑	SSIM↑	L1↓	PSNR↑	SSIM↑	L1↓
RayTracing	-	-	-	-	-	-	-	-	-	-	0.3300	-
VAE	21.54	0.7095	0.0656	22.90	0.7468	0.0612	23.51	0.7647	0.0549	18.62	0.7133	0.1033
DCGAN	22.41	0.7290	0.0600	21.66	0.7314	0.0625	22.55	0.7441	0.0559	18.81	0.7189	0.0967
NeRF ²	26.12	0.8122	0.0555	25.99	0.8004	0.0608	27.52	0.8118	0.0497	21.76	0.7732	0.0712
WRF-GS	25.53	0.7888	0.0514	26.10	0.7995	0.0534	24.00	0.7422	0.0534	20.72	0.7588	0.0788
Ours	30.75	0.9039	0.0410	30.17	0.9166	0.0442	32.96	0.9376	0.0355	24.75	0.8714	0.0582

Method	Conferenceroom (RX-moving)			Bedroom (RX-moving)			Office (RX-moving)			PSNR↑	Average	
	PSNR↑	SSIM↑	L1↓	PSNR↑	SSIM↑	L1↓	PSNR↑	SSIM↑	L1↓		SSIM↑	L1↓
RayTracing	-	-	-	-	-	-	-	-	-	-	-	-
VAE	23.93	0.7664	0.0524	22.57	0.7414	0.0609	22.75	0.7562	0.0612	22.26	0.7426	0.0656
DCGAN	21.26	0.7164	0.0608	21.79	0.7208	0.0601	20.95	0.7809	0.0529	21.35	0.7345	0.0641
NeRF ²	28.21	0.8528	0.0387	25.51	0.8057	0.0505	24.16	0.7863	0.0515	25.61	0.8203	0.0539
WRF-GS	26.64	0.7916	0.0423	25.50	0.7901	0.0482	24.07	0.7460	0.0510	24.65	0.7739	0.0541
Ours	30.54	0.9137	0.0315	28.15	0.9023	0.0398	28.01	0.8755	0.0406	29.33	0.9040	0.0417

real and imaginary parts of each spatial spectrum value are treated as separate channels during rasterization and are decomposed into magnitude and phase. We initialize the canonical space with 10k Gaussian primitives, and randomly distribute them in 2D spectrum space. Training follows a two-stage schedule: a coarse stage of 10k epochs to learn the canonical 2DGS representation, followed by a fine-tuning stage of 100k–150k epochs to optimize the deformation MLP. The deformation network is an eight-layer MLP with skip connections every two layers and a hidden width of 156 (See Fig. 5); positional encodings use 10 frequency bands for the primitive center and 6 for the moving transceiver position. All components are implemented in PyTorch and trained on an NVIDIA RTX 3090 GPU. Detailed hyperparameters are reported in Table 1.

6.2 Dataset

We evaluate our proposed framework on two types of datasets. The first is an open-source real-world dataset [13] collected in a laboratory environment equipped with tables, shelves, and partitioned rooms. A 4 × 4 antenna array operating at 915 MHz functions as the RX, while a passive RFID tag continuously transmits RN16 messages as the TX. The RX remains stationary, and the TX is systematically moved throughout the environment to capture varied spatial spectra. The second is our synthetic spatial spectrum dataset, which consists of three representative indoor scenes where the RX is also equipped with a 4 × 4 antenna array. Each scene contains two configurations under single-sided mobility. The real-world dataset provides a large-scale evaluation scenario with more complex geometric structures, whereas the synthetic datasets feature simpler environments, as illustrated in Fig. 6.

6.3 Benchmark

We evaluate SwiftWRF against a representative set of benchmarks, including the simulation-based ray-tracing method, deep-learning approaches (VAE and DCGAN), the implicit-neural-representation model NeRF², and the 3DGS solution WRF-GS.

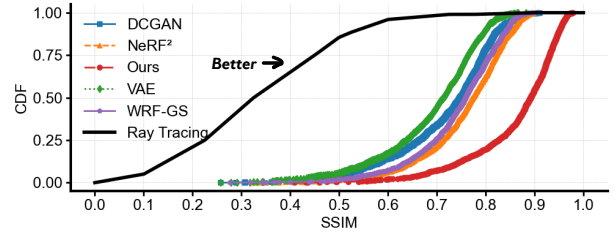


Fig. 7. CDF of SSIM on NeRF²-s23 dataset.

- **Ray Tracing [22]:** Ray tracing emits rays from the TX through each pixel of the scene model reconstructed from the point cloud to recursively model wireless propagation. We use MATLAB’s RayTracing toolkit to perform this simulation with high physical fidelity.
- **Variational Autoencoder (VAE) [8]:** A VAE learns to map observed data into a continuous latent space, from which new samples can be generated. In the context of WRF, the VAE is trained to predict the spatial spectrum at arbitrary TX locations based on discrete observations.
- **Deep Convolutional Generative Adversarial Network (DCGAN) [9]:** DCGAN consists of a convolutional generator and a convolutional discriminator trained in an adversarial loop. The generator aims to produce spectrum maps that resemble real measurements, while the discriminator learns to distinguish between real and synthesized outputs.
- **NeRF² [13]:** NeRF² models the WRF as a learnable volumetric density field. It encodes the scene density and signal strength into an MLP to render spatial spectra at arbitrary TX locations.
- **WRF-GS: [4]** WRF-GS is a GS-based method that leverages neural 3D Gaussian primitives for spectrum synthesis. It reconstructs spatial spectra at arbitrary TX positions by rasterizing learned Gaussians conditioned on TX location.

6.4 Metrics

We assess reconstruction quality with two complementary metrics. Peak signal-to-noise ratio (PSNR) [36] quantifies

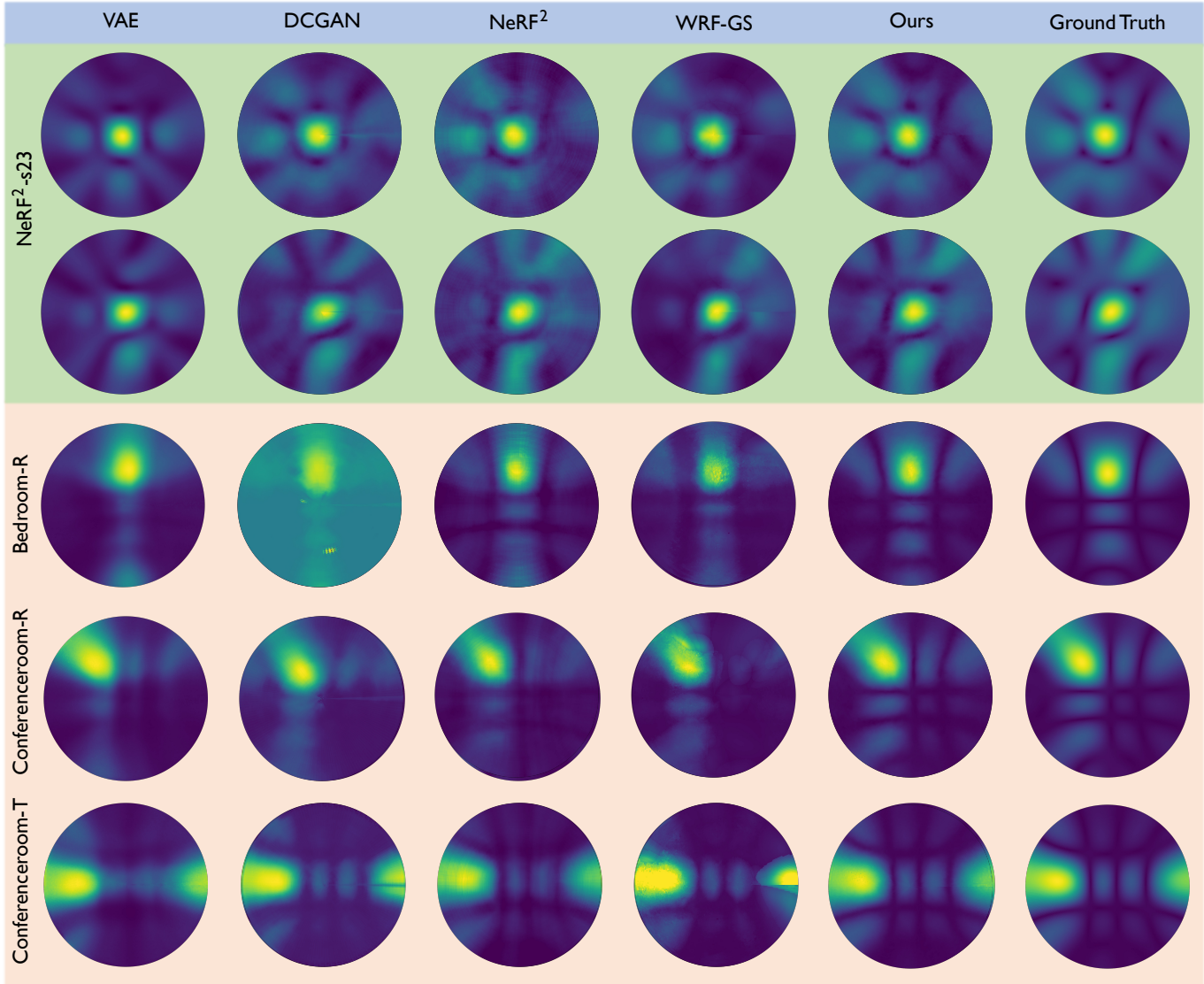


Fig. 8. Spectrum visualization on selected scenes (rendered at 90×360); please zoom in to see details.

pixel-wise fidelity by measuring the logarithmic ratio between the maximum possible signal power and the mean squared error; it is widely used in signal-reconstruction tasks to gauge absolute error levels. The structural similarity index measure (SSIM) evaluates perceived image quality by comparing local patterns of luminance, contrast, and structure [37]. We also report the L1 loss, which directly quantifies reconstruction accuracy by measuring the mean absolute per-pixel error. For computational efficiency, we report training time in hours and inference speed in seconds. Unless otherwise noted, all model parameters are stored in 32-bit floating point (FP32).

6.5 WRF reconstruction

To demonstrate the effectiveness of SwiftWRF, we first present per-scene evaluations against baseline methods across seven representative scenes. We then provide visual comparisons on selected examples to highlight qualitative differences. Finally, we report fast inference results on the

NeRF² dataset and analyze the impact of other contributing factors.

1) *Per-scene Evaluation*: Table 2 summarizes the evaluation metrics comparing our method against all baselines across all evaluated scenes, which include the large-scale real-world dataset NeRF² - s23 and the customized synthetic scenes. Overall, SwiftWRF achieves a PSNR improvement of 2.33–10.41 dB over competing methods, with consistent gains also observed in SSIM and l1 loss. On the large-scale NeRF² - s23 dataset, SwiftWRF achieves a PSNR improvement of 2.99–4.03 dB over both NeRF² and WRF-GS, and especially outperforms the ray tracing method with a 63% increase in SSIM. This is attributed to the fact that ray tracing relies heavily on geometric priors, and the LiDAR-based scene reconstruction may be insufficiently accurate. Fig. 7 presents cumulative SSIM curves across all evaluated positions, demonstrating that our method outperforms all baselines by a substantial margin. On synthetic scenes with simpler layouts, SwiftWRF consistently achieves superior results, with a PSNR improvement ranging from 2.65 dB

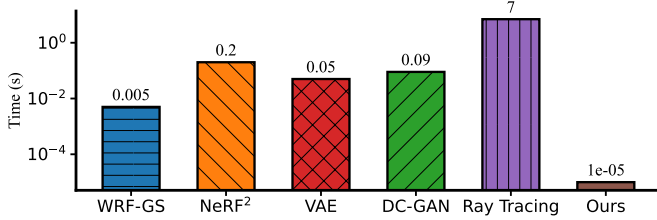


Fig. 9. Comparison of inference time for a single spectrum.

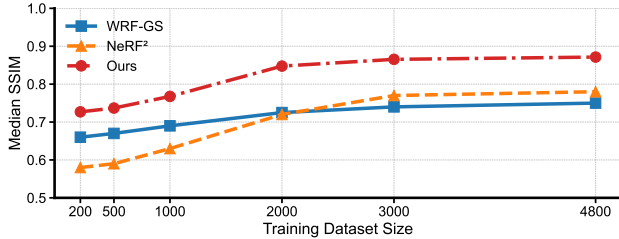


Fig. 10. Evaluation on different training scales.

to 10.41 dB over all baselines. Notably, the comparable performance observed under both mobility scenarios suggests that SwiftWRF captures two distinct types of field variation: in the RX-moving case, the MLP likely models spatial variations across different receiving positions, whereas in the TX-moving case, it captures temporal variations at a fixed location.

2) *Visual comparison*: A few toy examples from the visual comparisons are presented in Fig. 8 to highlight representative qualitative differences across methods. For clarity, we recommend zooming in to better observe reconstruction details. As shown, NeRF² produces ring-like blurring artifacts that degrade the overall signal spectrum. In contrast, WRF-GS exhibits localized blob-like noise patterns, likely caused by floaters introduced during the training of the 3DGS process. Meanwhile, traditional deep learning-based methods such as VAE and DCGAN yield heavily blurred results with limited structural fidelity. These visual observations further validate the superior quality of the signal maps generated by our method, in line with the objective metrics reported in Table 2.

3) *Efficiency*: We evaluate both the training and inference efficiency of a single-spectrum reconstruction across all methods on the NeRF² – s23 dataset, with results summarized in Fig. 9 and Fig. 11 (a). All methods are executed on a single NVIDIA RTX 3090 GPU, except for ray tracing. As shown in Fig. 9, our method achieves a substantial performance advantage, reaching approximately 100k FPS—over 500× faster than WRF-GS and more than 20,000× faster than NeRF². In addition, our model consistently outperforms both WRF-GS and NeRF² during training, achieving around 20% higher median SSIM across varying rendering times (see Fig. 11 (a)). This efficiency arises from our compact 2D Gaussian formulation, which enables highly parallelized CUDA-based rasterization without incurring the overhead of volumetric rendering in NeRF² or the Jacobian-based projection computations required by WRF-GS. Beyond its fast speed, SwiftWRF also delivers superior compactness,

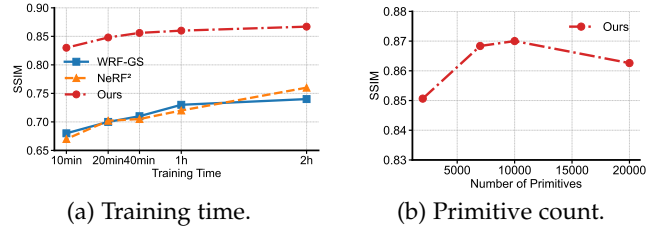


Fig. 11. Median SSIM under different conditions: (a) training time, and (b) primitive count.

TABLE 3
Ablation study of deformation components.

$\Delta\mu$	$\Delta\psi$	$\Delta\delta$	$\Delta\Sigma$	SSIM \uparrow / L1 \downarrow
✓	✓	✓	✗	0% / 0%
✓	✓	✓	✓	-19.10% / +86.44%
✓	✓	✗	✗	-15.73% / +69.49%
✓	✗	✓	✗	-1.22% / +1.69%
✗	✓	✓	✗	-3.37% / +13.56%

requiring only 1202 MB of GPU memory compared with 1804 MB for WRF-GS and 8978 MB for NeRF².

4) *Scale with training data*: To assess adaptability to limited training data, we compare SwiftWRF with NeRF² and WRF-GS across varying training set sizes. Specifically, we partition the original training set into subsets of different sizes [200, 500, 1000, 2000, 3000], and evaluate all models on the full test set to assess their robustness under limited data conditions. As shown in Fig. 10, the performance of all methods begins to saturate once the training size exceeds 3000 samples. Across all scales, SwiftWRF consistently outperforms both NeRF² and WRF-GS in terms of SSIM, demonstrating superior generalization under low-data regimes.

5) *Primitive count*: Another advantage of our framework is the ability to customize the number of primitives, allowing for flexible model scaling from lightweight to high-fidelity configurations, as illustrated in Fig. 11(b). Interestingly, increasing the primitive count beyond a certain threshold does not yield further quality improvements and may even lead to overfitting.

6.6 Ablation Study

In this section, we conduct a comprehensive ablation study of the SwiftWRF design. To validate the effectiveness of each design choice, the ablation is organized into two parts: (1) deformation components and (2) training protocols. For (1), as shown in Table 3, applying deformation to all components does not yield the best performance as initially expected. In particular, adding covariance deformation leads to an 86.44% increase in l1 loss, primarily due to the numerical instability it introduces by violating the lower triangular structure required for Cholesky decomposition. Excluding the covariance branch, all other deformation components contribute positively to performance, as verified through our step-wise ablation. Notably, position deformation proves to be the most critical, with its removal resulting in a 13.56% increase in l1 loss. Signal deformation has a relatively minor impact on reconstruction accuracy but still provides measurable gains in overall performance.

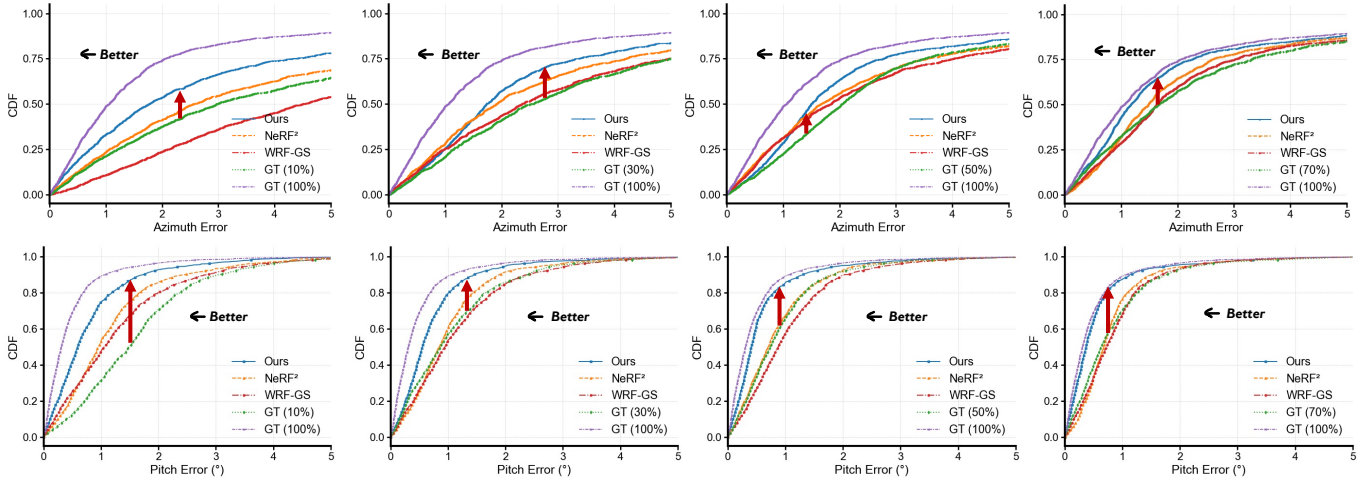


Fig. 12. CDF of AoA prediction error under four different mixture ratios. The red arrow represents the performance improvement achieved by incorporating novel spectra synthesized by SwiftWRF.

TABLE 4
Ablation study of training items.

Ablation items	SSIM \uparrow / L1 \downarrow	Training Time \downarrow
N/A	0% / 0%	0%
w/o Stop Gradient	+0.09% / +19.2%	+53.9%
w/o Coarse Training	+0.05% / -12.21%	-0.06%
w/o Anneal Smoothing	-0.17% / +2.72%	-3.79%
w/o SSIM Loss	-8.53% / +26.91%	-6.11%
w/ L2 Loss	-7.87% / +24.12%	+12.13%

These findings highlight the complementary roles of each component and confirm the optimality of our deformation design. For (2), the results reported in Table 4 show that applying stop-gradient significantly reduces training time, with only a marginal drop in reconstruction performance. All other training configurations have relatively minor impact on training speed, except for the use of l2 loss, which introduces a 12.13% overhead. The results also highlight that SSIM regularization and anneal smoothing reduce l1 loss to 2.72% and 26.91%, respectively, demonstrating their effectiveness in mitigating overfitting.

7 CASE STUDY

In this section, we present two representative case studies in the context of channel parameter prediction to demonstrate SwiftWRF’s adaptability to multi-tasking. The first case is AoA prediction, where we adopt a turbo-learning manner to showcase SwiftWRF’s capability for data augmentation. The second task is RSSI prediction, for which we adapt the output head of SwiftWRF to directly regress RSSI values.

7.1 AoA Prediction

Case setup: We perform AoA prediction using the Angular Artificial Neural Network (AANN)c [25], which is designed to learn the mapping between spatial spectra and their corresponding AoA values. To demonstrate SwiftWRF’s potential in reducing the burden of data collection, we compare two training strategies: turbo learning and naïve learning.

In the turbo learning setup, a portion of the ground-truth spectra is replaced with spectra generated by SwiftWRF, whereas in the naïve learning setup, the model is trained solely on the full set of ground-truth spectra. The AANN model is deployed using the ResNet-50 network [38], which is followed by an MLP for regression. The evaluation is conducted on the NeRF²-s23 dataset.

Results: Fig. 12 presents the CDF of azimuth and pitch angle prediction error under four turbo learning mixture ratios: 10%, 30%, 50%, and 70%.³ The purple curve labeled as GT (100%) represents the upper bound of prediction fidelity, obtained through the naïve training strategy described above. In contrast, the GT curves corresponding to each mixture ratio serve as theoretical lower bounds, as they retain only the specified proportion of the ground-truth training set. Fig. 12 uses red arrows to highlight the performance gains from SwiftWRF-generated spectra, with improvements of 18%, 21%, 16%, and 17% across the four ratios. As reported in Table 5, we further assess SwiftWRF’s effectiveness by comparing its turbo learning performance against NeRF² and WRF-GS under the same mixture ratios. Across all mixture ratios, SwiftWRF achieves the lowest median prediction errors in both pitch and azimuth. In particular, it outperforms NeRF² and WRF-GS in azimuth prediction with relative improvements ranging from 8.7%–30.6% and 19.2%–60.7%, respectively.

7.2 RSSI Prediction

Case setup: We adapt the output head of SwiftWRF for RSSI prediction by applying a global average pooling layer to the generated spectrum map, effectively aggregating directional information into a single RSSI value. The spectrum resolution is set to 16 \times 16, and the number of Gaussian primitives is reduced from 10k to 50 to ensure efficiency. For evaluation, we use a public BLE dataset [13], which contains RSSI measurements from multiple TXs at eight

3. The mixture ratio refers to the proportion of ground-truth spectra in the training set. For example, a 10% ratio indicates that only 10% of the samples are ground truth, while the remaining 90% are generated spectra.

TABLE 5
Median pitch and azimuth prediction errors (in degrees).

Ratio	SwiftWRF		NeRF ²		WRF-GS	
	Pitch ↓	Azimuth ↓	Pitch ↓	Azimuth ↓	Pitch ↓	Azimuth ↓
10%	0.5916	1.7691	0.9574	2.5479	1.0557	4.5064
30%	0.5527	1.7369	0.8496	1.9031	0.9477	2.3639
50%	0.4101	1.4978	0.7037	1.6628	0.8783	1.8541
70%	0.3697	1.1731	0.6738	1.4782	0.7272	1.6289

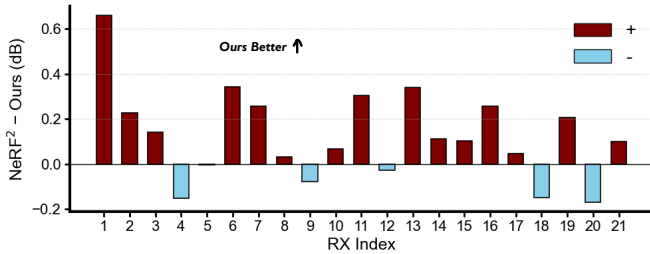


Fig. 13. L1 loss (dB) difference between Ours and NeRF².

fixed RX locations. A separate SwiftWRF model is trained for each RX position over 100k iterations. As a baseline, we include the MRI method [24], which estimates the RSSI at unsampled locations via interpolation based on a basic radio propagation model.

Result: For overall comparison, our method achieves the lowest median l1 loss of **2.91** dB, outperforming NeRF² at 3.05 dB and MRI at 6.74 dB. To further analyze performance at a finer granularity, we present a detailed per-RX comparison between SwiftWRF and NeRF² in Fig. 13. The plot shows the difference in median l1 error for each RX index, where positive bars indicate cases where SwiftWRF performs better. SwiftWRF outperforms NeRF² on the majority of RX positions, with significant margins observed at RX 1, 6, 11, and 13.

8 CONCLUSION

In this paper, we present SwiftWRF, a novel framework that adapts GS for WRF modeling. Compared to NeRF-based methods, GS eliminates the need for volumetric sampling and expensive MLP queries along rays, enabling significantly faster and more scalable spectrum reconstruction. On top of this, our reformulation into a 2D Gaussian primitive system further reduces redundancy inherent to 3D representations in single-sided transceiver mobility settings.

Contribution: SwiftWRF achieves high efficiency with reduced GPU memory consumption, enabling real-time spectrum synthesis at over 100k FPS and significantly faster training. Beyond spectrum reconstruction, it generalizes effectively to practical wireless tasks such as AoA and RSSI prediction, consistently outperforming existing baselines on both synthetic and real-world benchmarks. These results position GS as a promising new modeling paradigm for wireless propagation, effectively bridging the gap between geometry-driven simulations and data-driven field estimation.

Limitation: While SwiftWRF enables efficient spectrum reconstruction, its WRF representations are currently

trained offline. Incorporating online updates based on transceiver mobility could enable real-time channel estimation and enhance system adaptability. Additionally, although SwiftWRF delivers high-fidelity results in most cases, occasional synthesis failures indicate that further improvements in robustness and reconstruction quality remain necessary.

ACKNOWLEDGMENTS

This paper is supported by the National Natural Science Foundation of China (62371290, 62422111), National Key R&D Program of China (2024YFB2907204), STCSM under Grant (24511107100), Shanghai Key Lab of Digital Media Processing and Transmission, Shanghai Jiao Tong University and Shanghai Municipal Education Commission (No. 2024AIYB002).

REFERENCES

- [1] C. D. Alwis, A. Kalla, Q.-V. Pham, P. Kumar, K. Dev, W.-J. Hwang, and M. Liyanage, "Survey on 6g frontiers: Trends, applications, requirements, technologies and future research," *IEEE Open Journal of the Communications Society*, vol. 2, pp. 836–886, Feb. 2021.
- [2] D. C. Nguyen, M. Ding, P. N. Pathirana, A. Seneviratne, J. Li, D. Niyato, O. Dobre, and H. V. Poor, "6g internet of things: A comprehensive survey," *IEEE Internet of Things Journal*, vol. 9, no. 1, pp. 359–383, 2022.
- [3] M. Alsabah, M. A. Naser, B. M. Mahmmod, S. H. Abdulhussain, M. R. Eissa, A. Al-Baidhani, N. K. Noordin, S. M. Sait, K. A. Al-Utaibi, and F. Hashim, "6g wireless communications networks: A comprehensive survey," *IEEE Access*, vol. 9, pp. 148 191–148 243, 2021.
- [4] C. Wen, J. Tong, Y. Hu, Z. Lin, and J. Zhang, "Wrf-gs: Wireless radiation field reconstruction with 3d gaussian splatting," *arXiv preprint arXiv:2412.04832*, 2024.
- [5] M. Iskander and Z. Yun, "Propagation prediction models for wireless communication systems," *IEEE Transactions on Microwave Theory and Techniques*, vol. 50, no. 3, pp. 662–673, 2002.
- [6] T. Sarkar, Z. Ji, K. Kim, A. Medouri, and M. Salazar-Palma, "A survey of various propagation models for mobile communication," *IEEE Antennas and Propagation Magazine*, vol. 45, no. 3, pp. 51–82, 2003.
- [7] D. He, B. Ai, K. Guan, L. Wang, Z. Zhong, and T. Kürner, "The design and applications of high-performance ray-tracing simulation platform for 5g and beyond wireless communications: A tutorial," *IEEE communications surveys & tutorials*, vol. 21, no. 1, pp. 10–27, 2018.
- [8] D. P. Kingma, M. Welling *et al.*, "Auto-encoding variational bayes," 2013.
- [9] A. Radford, L. Metz, and S. Chintala, "Unsupervised representation learning with deep convolutional generative adversarial networks," *arXiv preprint arXiv:1511.06434*, 2015.
- [10] Z. Yuan, J. Luo, F. Shen, Z. Li, C. Liu, T. Mao, and Z. Wang, "DVP-MVS: Synergize Depth-Edge and Visibility Prior for Multi-View Stereo," 2024.
- [11] Z. Yuan, Z. Yang, Y. Cai, K. Wu, M. Liu, D. Zhang, H. Jiang, Z. Li, and Z. Wang, "Sed-mvs: Segmentation-driven and edge-aligned deformation multi-view stereo with depth restoration and occlusion constraint," *IEEE Transactions on Circuits and Systems for Video Technology*, 2025.
- [12] B. Mildenhall, P. P. Srinivasan, M. Tancik, J. T. Barron, R. Ramamoorthi, and R. Ng, "Nerf: Representing scenes as neural radiance fields for view synthesis," *Communications of the ACM*, vol. 65, no. 1, pp. 99–106, 2021.
- [13] X. Zhao, Z. An, Q. Pan, and L. Yang, "Nerf2: Neural radio-frequency radiance fields," in *Proceedings of the 29th Annual International Conference on Mobile Computing and Networking*, ser. ACM MobiCom '23. New York, NY, USA: Association for Computing Machinery, 2023. [Online]. Available: <https://doi.org/10.1145/3570361.3592527>

- [14] H. Lu, C. Vatttheuer, B. Mirzasoleiman, and O. Abari, "Newrf: A deep learning framework for wireless radiation field reconstruction and channel prediction," 2024. [Online]. Available: <https://arxiv.org/abs/2403.03241>
- [15] X. Chen, Z. Feng, K. Sun, K. Qian, and X. Zhang, "Rfcanvas: Modeling rf channel by fusing visual priors and few-shot rf measurements," in *Proceedings of the 22nd ACM Conference on Embedded Networked Sensor Systems*, 2024, pp. 464–477.
- [16] B. Kerbl, G. Kopanas, T. Leimkühler, and G. Drettakis, "3d gaussian splatting for real-time radiance field rendering," *ACM Trans. Graph.*, vol. 42, no. 4, pp. 139–1, 2023.
- [17] K. Yang, W. Du, and M. Srivastava, "Scalable 3d gaussian splatting-based rf signal spatial propagation modeling," in *Proceedings of the 23rd ACM Conference on Embedded Networked Sensor Systems*, 2025, pp. 680–681.
- [18] Z. Yang, X. Gao, W. Zhou, S. Jiao, Y. Zhang, and X. Jin, "Deformable 3d gaussians for high-fidelity monocular dynamic scene reconstruction," in *Proceedings of the IEEE/CVF conference on computer vision and pattern recognition*, 2024, pp. 20 331–20 341.
- [19] X. Zhang, X. Ge, T. Xu, D. He, Y. Wang, H. Qin, G. Lu, J. Geng, and J. Zhang, "Gaussianimage: 1000 fps image representation and compression by 2d gaussian splatting," in *European Conference on Computer Vision*. Springer, 2024, pp. 327–345.
- [20] C. Oestges, B. Clerckx, L. Raynaud, and D. Vanhoenacker-Janvier, "Deterministic channel modeling and performance simulation of microcellular wide-band communication systems," *IEEE Transactions on Vehicular Technology*, vol. 51, no. 6, pp. 1422–1430, 2002.
- [21] J. Tong, M. Jin, Q. Guo, and Y. Li, "Cooperative spectrum sensing: A blind and soft fusion detector," *IEEE Transactions on Wireless Communications*, vol. 17, no. 4, pp. 2726–2737, 2018.
- [22] Z. Yun and M. F. Iskander, "Ray tracing for radio propagation modeling: Principles and applications," *IEEE access*, vol. 3, pp. 1089–1100, 2015.
- [23] T. Orekondy, P. Kumar, S. Kadambi, H. Ye, J. Soriaga, and A. Bebbodi, "Winert: Towards neural ray tracing for wireless channel modelling and differentiable simulations," in *The Eleventh International Conference on Learning Representations*, 2023.
- [24] H. Shin, Y. Chon, Y. Kim, and H. Cha, "Mri: Model-based radio interpolation for indoor war-walking," *IEEE Transactions on Mobile Computing*, vol. 14, no. 6, pp. 1231–1244, 2015.
- [25] Z. An, Q. Lin, P. Li, and L. Yang, "General-purpose deep tracking platform across protocols for the internet of things," in *Proceedings of the 18th International Conference on Mobile Systems, Applications, and Services*, ser. MobiSys '20. New York, NY, USA: Association for Computing Machinery, 2020, p. 94–106. [Online]. Available: <https://doi.org/10.1145/3386901.3389029>
- [26] Y.-T. Sun, Y. Huang, L. Ma, X. Lyu, Y.-P. Cao, and X. Qi, "Splatter a video: Video gaussian representation for versatile processing," *Advances in Neural Information Processing Systems*, vol. 37, pp. 50 401–50 425, 2024.
- [27] G. Wu, T. Yi, J. Fang, L. Xie, X. Zhang, W. Wei, W. Liu, Q. Tian, and X. Wang, "4d gaussian splatting for real-time dynamic scene rendering," in *Proceedings of the IEEE/CVF conference on computer vision and pattern recognition*, 2024, pp. 20 310–20 320.
- [28] J. Tang, J. Ren, H. Zhou, Z. Liu, and G. Zeng, "Dreamgaussian: Generative gaussian splatting for efficient 3d content creation," *arXiv preprint arXiv:2309.16653*, 2023.
- [29] X. Zhou, Z. Lin, X. Shan, Y. Wang, D. Sun, and M.-H. Yang, "Drivinggaussian: Composite gaussian splatting for surrounding dynamic autonomous driving scenes," in *Proceedings of the IEEE/CVF conference on computer vision and pattern recognition*, 2024, pp. 21 634–21 643.
- [30] Z. Li, L. Yang, Y. Bian, H. Pan, Y. Fu, Y. Wang, Y.-C. Chen, G. Xue, and J. Ren, "Wideband rf radiance field modeling using frequency-embedded 3d gaussian splatting," *arXiv preprint arXiv:2505.20714*, 2025.
- [31] M. Liu, Q. Yang, M. Zhao, H. Huang, L. Yang, Z. Li, and Y. Xu, "D2gv: Deformable 2d gaussian splatting for video representation in 400fps," *arXiv preprint arXiv:2503.05600*, 2025.
- [32] B. Huang, Z. Yu, A. Chen, A. Geiger, and S. Gao, "2d gaussian splatting for geometrically accurate radiance fields," in *ACM SIGGRAPH 2024 conference papers*, 2024, pp. 1–11.
- [33] MATLAB, *Indoor MIMO-OFDM Communication Link Using Ray Tracing*, MathWorks, 2023, available at: <https://www.mathworks.com/help/comm/ug/indoormimo-ofdm-communication-link-using-raytracing.html>.
- [34] —, *Three-Dimensional Indoor Positioning with 802.11az Fingerprinting and Deep Learning*, MathWorks, 2023, available at: <https://www.mathworks.com/help/wlan/ug/threedimensional-indoor-positioning-with-802-11azfingerprinting-and-deep-learning.html>.
- [35] V. Ye, R. Li, J. Kerr, M. Turkulainen, B. Yi, Z. Pan, O. Seiskari, J. Ye, J. Hu, M. Tancik *et al.*, "gsplat: An open-source library for gaussian splatting," *Journal of Machine Learning Research*, vol. 26, no. 34, pp. 1–17, 2025.
- [36] J. Korhonen and J. You, "Peak signal-to-noise ratio revisited: Is simple beautiful?" in *2012 Fourth international workshop on quality of multimedia experience*. IEEE, 2012, pp. 37–38.
- [37] A. Hore and D. Ziou, "Image quality metrics: Psnr vs. ssim," in *2010 20th international conference on pattern recognition*. IEEE, 2010, pp. 2366–2369.
- [38] K. He, X. Zhang, S. Ren, and J. Sun, "Deep residual learning for image recognition," in *Proceedings of the IEEE conference on computer vision and pattern recognition*, 2016, pp. 770–778.



Mufan Liu received the B.Sc. degree in communication engineering from the University of Electronic Science and Technology of China, Chengdu, China, in 2023. He is currently pursuing the Ph.D. degree with the Cooperative MediaNet Innovation Center, Shanghai Jiao Tong University, Shanghai, China. His main research interests include adaptive streaming, joint source and channel coding and multimedia processing.



Cixiao Zhang received the B.Sc. degree in communication engineering from the University of Electronic Science and Technology of China, Chengdu, China, in 2023. He is currently pursuing the Ph.D. degree with the Cooperative MediaNet Innovation Center, Shanghai Jiao Tong University, Shanghai, China. His main research interests include Next-Generation Reconfigurable Antenna Systems, joint source and channel coding and multiple access technologies.



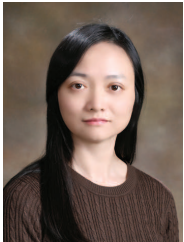
Qi Yang received the B.S. degree in communication engineering from Xidian University, Xi'an, China, in 2017, and Ph.D degree in information and communication engineering at Shanghai Jiao Tong University, Shanghai, China, 2022. He worked as a researcher in Tencent MediaLab from 2022 to 2024. Now, he joins University of Missouri–Kansas City as a research associate. He has published more than 35 conference and journal articles, including TPAMI, TIP, TVCG, TMM, TCSVT, ICML, CVPR, IJCAI, ACM MM, etc. He is also an active member in standard organizations, including MPEG, AOMedia, and AVS. His research interests include 3D/4D GS compact generation and compression, 3D point cloud and mesh quality assessment.



Yujie Cao received the B.Sc. degree in Information Engineering from Shanghai Jiao Tong University, Shanghai, China, in 2025. He is about to pursue the Ph.D. degree with the Cooperative MediaNet Innovation Center, Shanghai Jiao Tong University, Shanghai, China. His main research interests include semantic communications and 3DGS.



Shu Sun is a tenure-track associate professor in the School of Information Science and Electronic Engineering, Shanghai Jiao Tong University (SJTU), China. She obtained her B.S. degree in applied physics from SJTU in 2012 and Ph.D. degree in electrical engineering from New York University, USA, in 2018, and held summer internship positions at Nokia Bell Labs in 2014 and 2015. Shu also worked as a systems engineer at Intel Corporation. Her current research interests include channel modeling, millimeter-wave communications, integrated sensing and communication, and holographic MIMO. Dr. Sun received multiple international academic awards including the 2023 and 2017 IEEE Neil Shepherd Memorial Best Propagation Paper Awards, the 2017 Marconi Society Young Scholar Award, the IEEE VTC2016-Spring Best Paper Award, and the 2015 IEEE Donald G. Fink Award. She is an Associate Editor or Guest Editor of the IEEE TRANSACTIONS ON MOBILE COMPUTING, IEEE INTERNET OF THINGS MAGAZINE, and IEEE OPEN JOURNAL OF ANTENNAS AND PROPAGATION. She also served as a Guest Editor for the IEEE JOURNAL ON SELECTED AREAS IN COMMUNICATIONS.



Yiling Xu received the B.S., M.S., and Ph.D. degrees from the University of Electronic Science and Technology of China, in 1999, 2001, and 2004 respectively. From 2004 to 2013, she was a senior engineer with the Multimedia Communication Research Institute, Samsung Electronics Inc., South Korea. She joined Shanghai Jiao Tong University, where she is currently a professor in the areas of multimedia communication, 3D point cloud compression and assessment, system design, and network optimization. She

is the associate editor of the IEEE Transactions on Broadcasting. She is also an active member in standard organizations, including MPEG, 3GPP, and AVS.



Mingzeng Dai obtained his Master's degree in Telecommunication from Hangzhou Dianzi University in 2008. He is currently a Principal Researcher and 3GPP RAN2/3 delegate at the Wireless Research (WR) Lab of Lenovo Research. He has over 15 years' experience in 3GPP standardization as a key contributor in many technical areas of 4G and 5G. He also serves as the co-leader of the RS03 Native AI and Cross-Domain AI initiatives within the O-RAN nGRG. His research interests primarily focus on 6G RAN architecture, Integrated Sensing and Communication (ISAC), and AI/ML-enabled RAN.

on 6G RAN architecture, Integrated Sensing and Communication (ISAC), and AI/ML-enabled RAN.



Yin Xu received his B.Sc. degree in Information Science and Engineering from Southeast University, China, in 2009. Subsequently, he obtained his M.Sc. and Ph.D. degrees in Electronics Engineering from Shanghai Jiao Tong University (SJTU) in 2011 and 2015, respectively. In 2011, he served as a visiting scholar at McGill University and INRS. Currently, he is an Associate Professor and Ph.D. Supervisor at SJTU. His research interests span key technologies such as channel coding and modulation, new

waveforms, inter-tower communications, fluid/moveable antenna, and AI-assisted communications, along with the development of prototype systems for diverse communication systems including 5G/6G, satellite, broadcast, and short-range communications. He serves as an Associate Editor of Transactions on Broadcasting and is a recipient of the '6G Star Youth Scientist Award'. He also serves as co-chair, session chair, and keynote speaker at various major IEEE international conferences. Notably, he is actively involved in communication system standardization, serving as the chief 3GPP Standard delegate representing SJTU and holding the vice-chair position of Implementation Team 5 under the American Advanced Television Systems Committee (ATSC). His contributions to core physical layer technologies have been incorporated as key components into multiple globally reputable communication standards, including 3GPP 5G, ATSC 3.0, and SparkLink.



Yunfeng Guan received the Ph.D. degree from the Department of Electronics and Information Technology, Zhejiang University, Hangzhou, China, in 2003. Since 2003, he has been with the Institute of Wireless Communication Technology, Shanghai Jiao Tong University, where he is currently a Researcher with the Cooperative Medianet Innovation Center. His research interests include HDTV and wireless communications.